ROYAL AIRCRAFT ESTABLISHMENT
BEDFORD.

R. & M. No. 3306

MINISTRY OF AVIATION

AERONAUTICAL RESEARCH COUNCIL
REPORTS AND MEMORANDA

Experiments at $M = 1{\cdot}41$ on a Thin, Conically-Cambered Elliptic Cone of 30° Semi-Vertex Angle

By E. W. E. Rogers, V. G. Quincey and J. Callinan,
of the Aerodynamics Division, N.P.L.

LONDON: HER MAJESTY'S STATIONERY OFFICE
1963
ELEVEN SHILLINGS NET

Experiments at $M = 1 \cdot 41$ on a Thin, Conically-Cambered Elliptic Cone of 30° Semi-Vertex Angle

By E. W. E. Rogers, V. G. Quincey and J. Callinan,
of the Aerodynamics Division, N.P.L.

*Reports and Memoranda No. 3306**
August, 1961

Summary.

Pressure-plotting and strain-gauge balance tests have been made at a Mach number of 1·41 on a conically-cambered cone of 30° semi-vertex angle, and with a ratio of the major to the minor axis of its cross-section equal to 11·55. The camber line was designed for a C_L of 0·3 by the method of Ref. 2.

The upper-surface pressure distribution was found to be strongly influenced by the boundary-layer state in the leading-edge region, and when this was turbulent good agreement with the theoretical spanwise loading was obtained at the design C_L, though this was obtained at a somewhat higher incidence than the design value. The flow development with incidence for both boundary-layer states is discussed with the aid of oil-flow patterns.

The results for the cambered cone are compared with those obtained in 1954 for a corresponding uncambered elliptic cone. Both cones have the same normal-force curve slope; the cambered cone has a higher minimum drag coefficient, but a smaller lift-dependent drag factor. At the design C_L the drag of the two models is the same.

1. *Introduction.*

In 1954 tests were made at the N.P.L. on a series of elliptic cones of various thicknesses and semi-vertex angles. This work, at a stream Mach number of 1·41, is reported in Ref. 1. Many of the observed aerodynamic characteristics could be related to the onset and subsequent development of a leading-edge separation when the models were at incidence, and at the time it was felt that some improvement at moderate lift might result from cambering the major axis of the cone and by this means delaying to a higher incidence the first occurrence of separation.

Later, Brebner[2] discussed some simple conical-camber shapes designed to produce zero load at the leading edge at the design lift coefficient. Accordingly a cambered elliptic cone was made, having a design C_L of 0·3; the thickness distribution was that of a symmetric elliptic cone tested earlier (cone C2 of Ref. 1). The present report considers the aerodynamic behaviour of the cambered cone and compares this with that of the uncambered cone.

Most of the material presented was obtained at intervals between March and June, 1961. Some use has been made, however, of data from the 1954 tests.

* Previously issued as A.R.C. 23,329. Published with the permission of the Director, National Physical Laboratory.

2. *Experimental Details.*

2.1. *The Tunnel.*

The tests were carried out in the N.P.L. 18 in. by 14 in. High Speed Wind Tunnel, at a stream Mach number of 1·41. The test region had been previously calibrated and found to be free from serious error, the extreme values of local Mach number in the volume occupied by the model were 1·40 and 1·42; a mean value of 1·41 was therefore used. The stagnation pressure of the tunnel flow was maintained constant at 31 in. mercury absolute throughout the experiment, giving a Reynolds number based on the centre-line chord of the model, of $2 \cdot 0 \times 10^6$. Both the cambered and the plain cone were supported from their bases by a slender rectangular sting (Fig. 1). Two stings were used, one for the pressure-plotting tests and the other, incorporating a three-component strain-gauge balance, for finding the overall lift and drag acting on the cone.

Incidence (α) was applied to the models in the plane containing the minor axis of the elliptic cross-section (i.e., in a similar manner to that for a wing of the same planform). The position of the sting was adjusted to maintain the centre of the model fixed with respect to the working section throughout the incidence range.

2.2. *The Models.*

The plain, or uncambered, cone was that used in the tests reported in Ref. 1. Its planform had a semi-vertex angle (ϵ) of 30° and an aspect ratio of 2·31. The ratio (μ) of the major to the minor axis of the elliptic cross-section was 11·55 and at the blunt base the ratio (τ) of the minor axis to the centre-line chord (c_0) was 0·10; the latter dimension was 5·0 in. The model was made of steel and had 34 pressure-plotting holes on the curved surfaces and a further 8 distributed along the base; details of their disposition will be found in Ref. 1.

The cambered cone had the same planform and values of μ and τ, but outboard of 0·70 semispan ($\eta = 0 \cdot 7$) the profile was conically cambered. The camber line of the cone cross-section is given by equation (23) of Ref. 2 with $\bar{\eta} = 0 \cdot 7$, a design C_L (or C_N) of 0·3 and the parameter K put equal to tan 30°. The camber-line equation then reduces to

$$\frac{z_c}{c_0} = A\left(\bar{\eta}^2 - \eta^2 - 2\eta\bar{\eta}\log_e\frac{\bar{\eta}}{\eta}\right), \tag{1}$$

where

$$A = \frac{C_L}{K}\,\frac{3}{3\cos^{-1}\bar{\eta} - \bar{\eta}(5-2\bar{\eta}^2)\sqrt{(1-\bar{\eta}^2)}} = 4 \cdot 139 \text{ in this case;}$$

z_c is measured normal to the major axis of an uncambered cone. The elliptic thickness distribution was added directly to the camber ordinate so that for any spanwise station, η, the value of z on the upper and lower surfaces of the cone is given by

$$\frac{z}{c_0} = \frac{z_c}{c_0} \pm \tfrac{1}{2}\tau\sqrt{(1-\eta^2)}. \tag{2}$$

The surface ordinates are listed in Table 1, and the cambered and uncambered profiles are compared in Fig. 2.

The cambered cone was made of steel and contained 37 pressure holes on the curved surfaces and 6 on the blunt base, distributed along the camber line. Their positions are shown diagrammatically

in Fig. 3 and are listed in Table 2. Some check on the conical nature of the surface flow could be obtained on the upper surface by comparing the readings of 3 holes (Nos. 12a, b, c) lying along a ray passing through the vertex and corresponding to $\eta = 0 \cdot 8$.

2.3. *Experimental Method and Reduction of the Observations.*

2.3.1. *Pressure measurements.*—The pressure distributions were measured simultaneously on both surfaces of the cambered cone. The incidence range ($-7°$ to $+9°$) was limited by the maximum permitted bending stress in the supporting sting. The sting deflected under the aerodynamic load, and a correction (found optically) was therefore applied to the nominal incidence. Two sets of pressure distributions were obtained with the cambered cone. In one of these boundary-layer transition was allowed to occur naturally; in the other a roughness band, containing sieved No. 200 grade carborundum powder set in a lacquer, extended along both leading edges on the cone upper surface, from 2% to 8% of the local semispan. This caused immediate transition to turbulent boundary-layer flow at all incidences tested, approximately $-1°$ to $+9°$ for this condition. The surface pressure readings were reduced to C_p in the usual way.

No pressure measurements were made on the uncambered cone during the present tests, because of the existence of data obtained in 1954 for both boundary-layer states in the same tunnel at the same Mach number.

If the flow about the cones is assumed to be conical, the values of C_p on the curved surfaces may be plotted against η and then integrated to give the normal pressure-force coefficient C_{Np} for the cone. The variation in C_p along the ray $\eta = 0 \cdot 8$ was very small; nevertheless in the integrations, and in the pressure distributions presented in this report, the value obtained at $x/c_0 = 0 \cdot 84$ was used, as this lies closest to the main group of pressure holes. Strictly the normal force derived from the integration corresponds to some average value over a region between about $0 \cdot 6$ and $0 \cdot 85$ of the centre-line chord.

The chordwise or axial pressure-force coefficient (C_{Xp}) may similarly be obtained by integrating the projection of the surface pressures on the base. In the general case

$$C_{Xp} = \tfrac{1}{2} \tan \epsilon \int_0^{2\pi} C_p \left[\left(\frac{y}{a}\right)^2 + \left(\frac{z}{a}\right)^2 \right] d\theta \tag{3}$$

where θ ($= \tan^{-1} z/y$) is measured from the centre of the base section, and a is the semispan. If the cross-section is a true ellipse this equation simplifies to

$$C_{Xp} = \tfrac{1}{2} \tan \epsilon \int_0^{2\pi} \frac{C_p \, d\theta}{1 + (\mu^2 - 1) \sin^2 \theta}. \tag{4}$$

Because of the complex form of the camber-line equation in the case of the cambered cone, equation (3) with the local values of y and z was used, and the integration was performed mechanically.

The related lift and pressure-drag coefficients, C_{Lp} and C_{Dp}, can be found by resolution from C_{Np} and C_{Xp}.

The pressure over the base of the cambered cone was measured for a range of incidence both with and without the upper-surface roughness band. Because the 6 base holes are set in pairs symmetrically about the mid-span position the mean recorded pressure of the holes on the right- and left-hand sides of the model has been used to form the base-pressure coefficient $\overline{C}_{pb}$. The differences between the two sides were quite small and no serious error is introduced by taking a mean value.

2.3.2. *Balance tests.*—With the balance sting, direct measurements were made of the overall normal and axial forces on the cambered cone, primarily to check the accuracy of the pressure integrations, and the implicit assumption of conical flow. The balance sting also deflects under aerodynamic load and a correction has been applied to the nominal incidence.

The balance normal force includes the force on a small part of the sting itself and also the force on the pressure leads which extend a short distance downstream of the cone base. Thus some correction is necessary in order to obtain a force coefficient comparable with C_{Np}. This correction is small, however, reaching about 2% of the measured value at the highest incidence.

The recorded balance axial force consists of the axial pressure force on the curved surfaces of the cone (C_{Xb}, corresponding to C_{Xp}), the surface friction on this area, the base force and the contributions to the axial force due to the exposed portion of the sting and the pressure leads. Estimates of these components must be made before a comparison can be obtained between C_{Xb} and C_{Xp}; it is clear that some uncertainty will exist in the value attributed to the former coefficient. No balance measurements were made on the cambered cone with a roughness band or on the uncambered cone; in the latter case earlier data were available, if required.

2.3.3. *Oil-flow patterns.*—Surface flow patterns using a titanium oxide and oil mixture were photographed for the full incidence range on both surfaces of the cambered cone, with and without the roughness band. Because of the unsatisfactory nature of the oil patterns originally obtained with the plain elliptic cone, these were repeated. The surface flow patterns were used not only to study the development of the boundary-layer separation and shock waves but also to check the efficacy of the roughness band in promoting transition.

3. *Results.*

3.1. *Spanwise Pressure Distributions.*

The spanwise distribution of pressure on the upper surface of the cambered cone is shown in Fig. 4a when natural boundary-layer transition was permitted, and in Fig. 4b when transition occurred at the roughness band. The lower-surface distributions are shown in Fig. 4c. For comparison purposes the spanwise pressure distributions on the uncambered elliptic cone have been plotted in Fig. 5.

The development of the upper-surface flow can be interpreted in some measure with the aid of the oil-flow patterns. With no roughness band and at zero incidence there is attached flow over all the surface; the laminar boundary layer is confined to a region upstream of about $x/c_0 = 0 \cdot 5$ (Fig. 6a). At $\alpha = 2 \cdot 1°$ a disturbance forms near $\eta = 0 \cdot 8$, which may either be a very local boundary-layer separation or thickening, or a weak shock wave. It is difficult to distinguish these phenomena in the present case from only the oil-flow patterns and pressure distributions; oblique-beam shadow or schlieren photographs[1] are really required. At $\alpha = 2 \cdot 1°$, the local Mach number component normal to the disturbance is about $1 \cdot 06$ so that a weak shock wave would appear possible; on the other hand the local Mach number at the disturbance is very close to the free-stream value and there is little sign of a shock wave at this incidence when the boundary layer is turbulent from the leading edge. A well-marked laminar separation, followed by turbulent reattachment, is clearly visible at $\alpha = 3 \cdot 2°$, and there is doubtless a shock wave associated with this flow separation. It is not possible to say whether the separation arises initially because of the presence of a shock wave in the flow about the model, or whether it occurs because of the flow deflections inherent in the separation process, an event which may then be regarded as due to the locally unfavourable pressure gradients.

The reattachment line moves slowly inboard with increasing incidence and a vortex structure in the separated layer is visible at $\alpha = 5 \cdot 4°$, becoming more pronounced at higher angles. At all incidences the flow is attached between the leading edge and some position inboard of $\eta = 0 \cdot 9$, though presumably at a sufficiently high incidence, beyond the present test range, the separation line would move outboard to the leading edge.

When the boundary layer is made turbulent a shock wave cannot be detected in the oil-flow patterns until the incidence is above about 6°, and separation to the rear of a well-defined shock is delayed to near $\alpha = 7°$. The separation line is slightly further inboard than for the transition-free case but this difference may be partly due to the oil boundary in the latter condition indicating a separation position which is somewhat outboard of the actual shock.

On the lower surface, flow separation occurs at the leading edge for all incidences below about $6 \cdot 5°$. There is a pronounced vortex structure particularly at incidences below 2°, the reattachment line and the secondary separation line being well marked. Except above $\alpha = 6 \cdot 5°$ (Fig. 6b) the boundary-layer flow over the entire lower surface was turbulent. The effect of the upper-surface roughness band on the lower-surface flow should be negligible, except when the cone is at a sufficiently high negative incidence for the stagnation line to move round the leading edge onto the band, a condition not achieved in the present tests. Fig. 4c indicates that in general the agreement between the two sets of results on the lower surface was good, the observed differences being comparatively small.

The pressure distributions for the plain cone (Fig. 5) show the development with incidence of a leading-edge separation and associated vortex, as described in Ref. 1. No significant differences were then found when a roughness band was placed in the leading-edge region.

The flow boundaries for the cambered cone without the roughness band are set out in Fig. 7a, and those for the upper surface are replotted in Fig. 7b and compared with similar boundaries for the plain cone and the cambered cone with a roughness band. At the design C_L the lower-surface separation has just been suppressed, and for a turbulent boundary layer on the upper surface, separation is again absent; in fact the condition of no separation on either surface exists in a very limited range near the design C_L.

The spanwise pressure distributions for the cambered cone in the two boundary-layer states at a lift coefficient close to the design value are compared in Fig. 8. Between the leading edge and $\eta = 0 \cdot 85$ the two distributions agree closely. The most marked differences occur for η between $0 \cdot 5$ and $0 \cdot 75$ and these resemble those obtained on two-dimensional aerofoils when a normal shock wave interacts with either a laminar or a turbulent boundary layer. The net effect of the change in pressure distribution shape with boundary-layer state is to make the normal-force coefficient slightly larger in the transition-free condition. By comparison the plain cone achieves a value of C_L equal to the design value at a lower geometric incidence, and in Fig. 8 a distribution corresponding to a C_{Np} of $0 \cdot 298$ is plotted. Much higher velocities are attained on the upper surface close to the leading edge and also towards the centre of the section. On the lower surface a rather higher pressure occurs close to the leading edge but this effect is reversed over a considerable portion of the semispan inboard of $\eta = 0 \cdot 9$. The development of the upper-surface peak suction with model incidence is strikingly different for the cambered and uncambered cones, as Fig. 9 shows. The onset of separation however is not directly related to the attainment of any particular value of C_p, even for a given boundary-layer state. Separation on the plain cone takes place at the leading edge, and on the cambered cone further inboard.

Fig. 9 also shows that at low incidences the minimum pressures obtained for both states of the cambered cone are different. This is illustrated in more detail in Fig. 10 for a typical incidence of $-0 \cdot 1°$. On the lower surface the two distributions agree closely but outboard of $\eta = 0 \cdot 5$ on the upper surface the velocities are lower when the boundary layer is turbulent. This change cannot be attributed to some modification of a flow separation by the roughness band, because the upper-surface flow is everywhere attached at this incidence. No convincing reason for the discrepancy has been forthcoming and as will be seen in Fig. 8 the effect tends to disappear at the higher incidences.

The three distributions used in Fig. 8 are presented as loadings in Fig. 11, in terms of $\Delta C_p / C_{Np}$ and the theoretical curve of Ref. 2 is also included. The latter agrees reasonably well with the experimental curve for the cambered cone with a turbulent boundary layer, though the peak theoretical loading is slightly lower and occurs rather closer to the leading edge. It is perhaps necessary to note that the comparison is made at about the same C_N, and does not represent the conditions obtained at the theoretical design incidence; the latter ($5 \cdot 7°$) gives a normal force which is smaller than required theoretically (*see* Section 3.2 below) and a somewhat different loading. The loading curves change shape as the lift alters from the design value (Fig. 12), and for the cambered cone the effect of the lower-surface separation at negative incidences is most marked.

3.2. *Forces.*

The normal-force coefficients, based on the assumption of conical flow and obtained from integrating the pressure distributions, are shown in Fig. 13a. As would be expected from the type of differences in the pressure distributions for the two boundary-layer conditions, the values of C_{Np} at a given incidence are slightly different. This effect is most marked at the highest incidences and the larger normal force for the transition-free case is associated almost entirely with more inboard reattachment position and the consequent inboard extension of the low-pressure region under the vortex. This effect more than outweighs the reduction in normal force due to the smaller peak suction.

The normal-force slope with cone incidence at small values of C_{Np} is close to that obtained for the plain cone and that predicted for a flat-plate wing of the same planform. The effect of the camber is to give zero normal force at a positive geometric incidence, a fact noted by Michael in Ref. 3. The design C_L (or C_N) is achieved at an incidence close to 7°; the value predicted by Brebner in Ref. 1 is about $5 \cdot 7°$. The difference between the observed and theoretical values of the design incidence is probably due to the use of slender-wing theory by Brebner, and hence a lift-curve slope somewhat larger than that actually attained (*see* Fig. 13a).

The normal-force curve for the transition-free condition may be compared with the measured balance values after these have been corrected for the influence of the exposed sting and pressure leads (Fig. 13b). The agreement between the two sets of results is satisfactory and suggests that the assumption of conical flow about the model is reasonable. This conclusion supports the evidence of the pressure readings obtained along the line $\eta = 0 \cdot 8$.

The axial pressure-force coefficients C_{Xp} obtained by integration are shown in Fig. 14, where they may be compared with similar results for the uncambered cone. Near zero incidence the value of C_{Xp} is considerably higher when the cone is cambered, but the subsequent decrease with incidence is far more rapid, suggesting that the lift-dependent drag factor is smaller. The effect of a roughness band is to increase C_{Xp} at low incidence and to reduce it at high incidence. These trends are consistent with the differences in the pressure distributions noted earlier.

The values of C_{Dp} obtained by resolution of C_{Xp} and C_{Np} show that on the cambered cone the minimum value of C_{Dp} occurs near $\alpha = 2°$, and that above $\alpha = 5°$ the pressure drag is lower than on the plain cone. This comparison is best made on the basis of the cone normal force, as in Fig. 15, where it will be seen that the cambered cone has a lower value of C_{Dp} above the design lift coefficient. The lift-dependent drag of the cambered cone is clearly lower than on the plain cone. If a lift-dependent drag factor (K) is defined by

$$K = \frac{\pi A}{C_{Lp}^2} [C_{Dp} - (C_{Dp})_{\min}]$$

where A is the planform aspect ratio, then at $C_{Lp} = 0 \cdot 3$, K has a value of $1 \cdot 4$ for the cambered cone with a turbulent boundary layer compared with $2 \cdot 0$ for the plain cone. This implies that the lift-dependent drag performance of the cambered cone is considerably better than that of the plain cone. This conclusion needs some qualification since the effect is partly due to the higher value of $(C_{Dp})_{\min}$ for the cambered model, associated in some measure with the lower-surface separation visible in Fig. 6a. This is suppressed as the incidence is increased and a reduction of K results. An alternative method of defining a lift-dependent drag factor (K') uses the drag of the corresponding uncambered cone at zero lift in place of $(C_{Dp})_{\min}$. Thus

$$K' = \frac{\pi A}{C_{Lp}^2} [C_{Dp} - (C_{D0})_{\text{uncambered}}]$$

This approach would yield no difference in the lift-dependent drag factors of the cambered and uncambered cones at the design C_L; K' is smaller for lift coefficients above $0 \cdot 3$.

Finally the pressure-force results may be plotted in terms of the ratio C_{Lp}/C_{Dp} (Fig. 16). The plain cone achieves a slightly higher maximum value of this ratio, but near the design lift coefficient there is little difference in the three cases.

As explained in Section 2.3.2 it is possible to estimate approximately from the total axial force measured on the balance, the pressure-drag coefficient for the forward-facing curved surfaces. This is only a small part of the measured axial-force coefficient and will not be very precise. Fig. 17 does suggest however that the integrated values of C_{Xp} are reasonably valid, and further indicates the large contribution of the base pressures to the overall axial force.

3.3. *Base Pressures.*

The values of the mean base-pressure coefficient $\bar{C}_{pb}$ obtained on the cambered cone at $\eta = 0 \cdot 774$ are compared with those for the plain cone (with no roughness band) at $\eta = 0 \cdot 70$, the nearest available pressure-hole position. The latter results agree closely with those for the cambered cone in the transition-free state, except at the higher incidences. When a roughness band is added there is a small increase in $\bar{C}_{pb}$.

With the few pressure holes available it is not possible to find accurately the spanwise variation of base pressure, but this does not appear to be very large (Fig. 18b) though some increase in transverse pressure gradient occurs as the cone incidence is increased or decreased from a near-zero value. It seems reasonable to attribute this effect to the development of shock waves and flow separations on the cone surface.

The general level of the base pressures and their variation with incidence are similar to those reported by Stivers and Levy[4] for stations on the base of an elliptic cone with $\epsilon = 15°$, $\mu = 3$, when tested at a stream Mach number of $1 \cdot 40$.

4. *Concluding Remarks.*

The present tests have shown that it is possible to obtain good agreement between the theoretical and experimental loadings at the design C_L for a cambered elliptic-cone model, and that the condition of zero loading at the leading edge can be achieved. In the experiment a separation occurred near the maximum-velocity position on the upper surface when the boundary layer was laminar, and this caused a severe modification of the surface pressure distribution and consequently the spanwise loading. It is uncertain whether this separation is directly caused by the presence of a forward shock wave on the model surface or whether it arises because of the adverse pressure gradients to the rear of the peak suction. With a turbulent boundary layer a forward shock wave cannot be detected until a somewhat higher incidence, and shock-induced separation of the boundary layer takes place* just above the incidence at which the design lift occurs. Near this condition the differences in the shape of the upper-surface pressure distributions for the two boundary-layer states are very similar to those observed on two-dimensional aerofoils at transonic speeds.

The other marked feature of the flow about the cambered cone is the vortex that develops under the drooped lower surface at incidences below that at which the design lift is attained. This flow separation must contribute to the high minimum drag of the cambered cone, and some improvement might result if the design C_L were reduced, since the amount of leading-edge droop is directly proportional to this quantity. The position at which the camber begins ($\bar{\eta} = 0 \cdot 7$) is very close to that giving the minimum camber-line slope at the leading edge so there would appear to be little to gain from changing the value of $\bar{\eta}$. Some reduction in the design C_L would also lower the upper-surface velocities in the leading-edge region, thus delaying the appearance of the forward shock and the local flow separations. Alternatively some relief might be obtained from a reduction in the profile thickness.

Compared with the plain elliptic cone, the cambered cone has the same lift-curve slope, but achieves the design C_L at a somewhat higher incidence. The minimum drag is greater, but the lift-dependent drag factor is smaller, so that at the design lift the drag of the two models is nearly the same. The difference in the two values of the lift-dependent drag factor is partly associated with suppression of the lower-surface separation as the incidence increases and partly a reflection of the comparatively small changes in the general shape of the pressure distributions with incidence for the cambered cone; when the cone is uncambered the effect of incidence is to modify most markedly the distribution that occurs at zero lift.

5. *Acknowledgment.*

The authors wish to acknowledge the assistance given by Dr. R. C. Lock of the N.P.L. in the design of the cambered cone and in subsequent discussions of the results.

---

* The local Mach number component normal to the shock front at incipient separation is about $1 \cdot 36$, a value consistent with those obtained in Ref. 5 and elsewhere.

REFERENCES

No.	Author	Title, etc.
1	E. W. E. Rogers and C. J. Berry	Experiments at $M = 1 \cdot 41$ on elliptic cones with subsonic leading edges. A.R.C. R. & M. 3042. October, 1955.
2	G. G. Brebner	Some simple conical camber shapes to produce low lift-dependent drag on a slender delta wing. A.R.C. C.P.428. September, 1957.
3	W. H. Michael	Flow studies on drooped-leading-edge delta wings at supersonic speed. N.A.C.A. T.N.3614. January, 1956.
4	L. S. Stivers and L. L. Levy ..	Effects of sting-support diameter on the base pressures of an elliptic cone at Mach numbers from $0 \cdot 60$ to $1 \cdot 40$. N.A.C.A. T.N. D-354. February, 1961.
5	E. W. E. Rogers, C. J. Berry and J. E. G. Townsend	A study of the effect of leading-edge modifications on the flow over a 50° sweptback wing at transonic speeds. A.R.C. R. & M. 3270. May, 1960.

TABLE 1

Profile Ordinates

η	y/c_0	z/c_0	
		Upper surface	Lower surface
0	0	0·05	−0·05
0·1	0·0577	0·04975	−0·04975
0·2	0·1155	0·04899	−0·04899
0·3	0·1732	0·04770	−0·04770
0·35	0·2021	0·04684	−0·04684
0·4	0·2309	0·04583	−0·04583
0·45	0·2598	0·04465	−0·04465
0·5	0·2887	0·04330	−0·04330
0·55	0·3175	0·04176	−0·04176
0·6	0·3464	0·04000	−0·04000
0·65	0·3753	0·03800	−0·03800
0·7	0·4041	0·03571	−0·03571
0·72	0·4157	0·03468	−0·03472
0·74	0·4272	0·03351	−0·03375
0·76	0·4388	0·03209	−0·03291
0·78	0·4503	0·03034	−0·03224
0·80	0·4619	0·02816	−0·03184
0·82	0·4734	0·02548	−0·03176
0·84	0·4850	0·02221	−0·03205
0·86	0·4965	0·01825	−0·03277
0·88	0·5081	0·01357	−0·03396
0·90	0·5196	0·00795	−0·03563
0·92	0·5312	0·00139	−0·03781
0·94	0·5427	−0·00630	−0·04042
0·96	0·5543	−0·01536	−0·04336
0·98	0·5658	−0·02631	−0·04621
0·99	0·5716	−0·03301	−0·04711
0·995	0·5745	−0·03706	−0·04704
1·0	0·5774	−0·04410	−0·04410

η is the fraction of the local semispan measured from the centre of the cross-section towards the tip.

y and z are the distances along the major and minor axes of the cross-section.

c_0 is the mid-span chord of the cone.

TABLE 2

Pressure-Hole Positions

(*a*) *On the Curved Surfaces.*

Upper surface			Lower surface		
Hole No.	η	x/c_0	Hole No.	η	x/c_0
1	1·0	0·75	18	1·0	0·75
2	0·997	0·83	19	0·997	0·67
3	0·995	0·72	20	0·995	0·72
4	0·990	0·63	21	0·990	0·81
5	0·985	0·79	22	0·985	0·83
6	0·980	0·69	23	0·980	0·63
7	0·970	0·79	24	0·970	0·65
8	0·950	0·73	25	0·950	0·67
9	0·925	0·74	26	0·925	0·78
10	0·90	0·70	27	0·90	0·79
11	0·85	0·69	28	0·85	0·72
12a	0·80	0·84	29	0·80	0·74
12b	0·80	0·50	30	0·75	0·63
12c	0·80	0·25	31	0·70	0·63
12d	0·80	0·84	32	0·60	0·68
13	0·75	0·68	33	0·40	0·65
14	0·70	0·65	34	0	0·68
15	0·60	0·67			
16	0·40	0·82			
17	0	0·75			

x is the distance from the cone vertex towards the base.

(*b*) *On the base.*

Hole No.	η
B1, B4	0·562
B2, B5	0·774
B3, B6	0·942

All base-pressure holes are on the camber line of the base.

Holes B1, B2, B3 are on the left-hand side of the base; holes B4, B5, B6 are on the right-hand side.

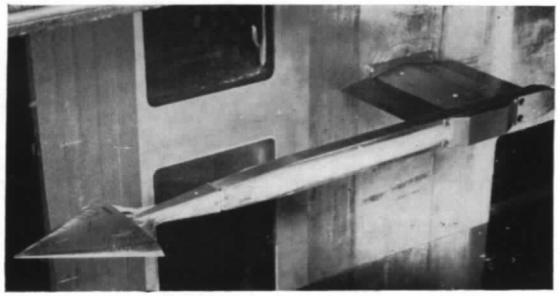

FIG. 1. Model and sting mounting in 18 in. × 14 in. Tunnel.

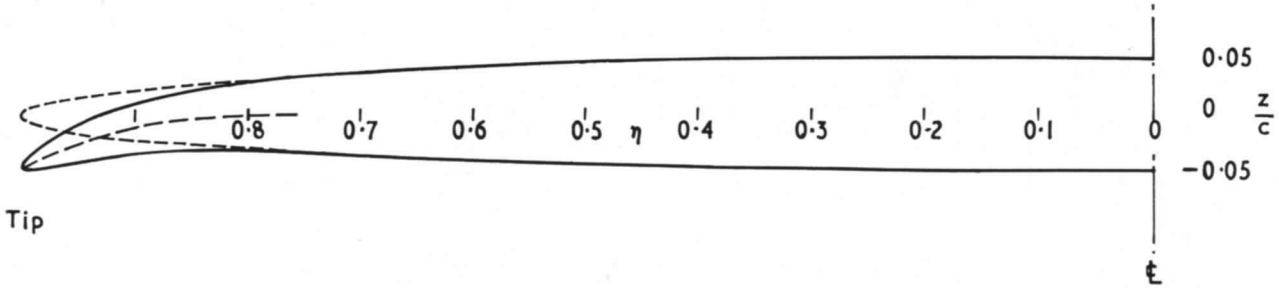

FIG. 2. Comparison of cross-sections of cambered and uncambered elliptic cones; η denotes the fraction of the local semispan, c the distance from the vertex.

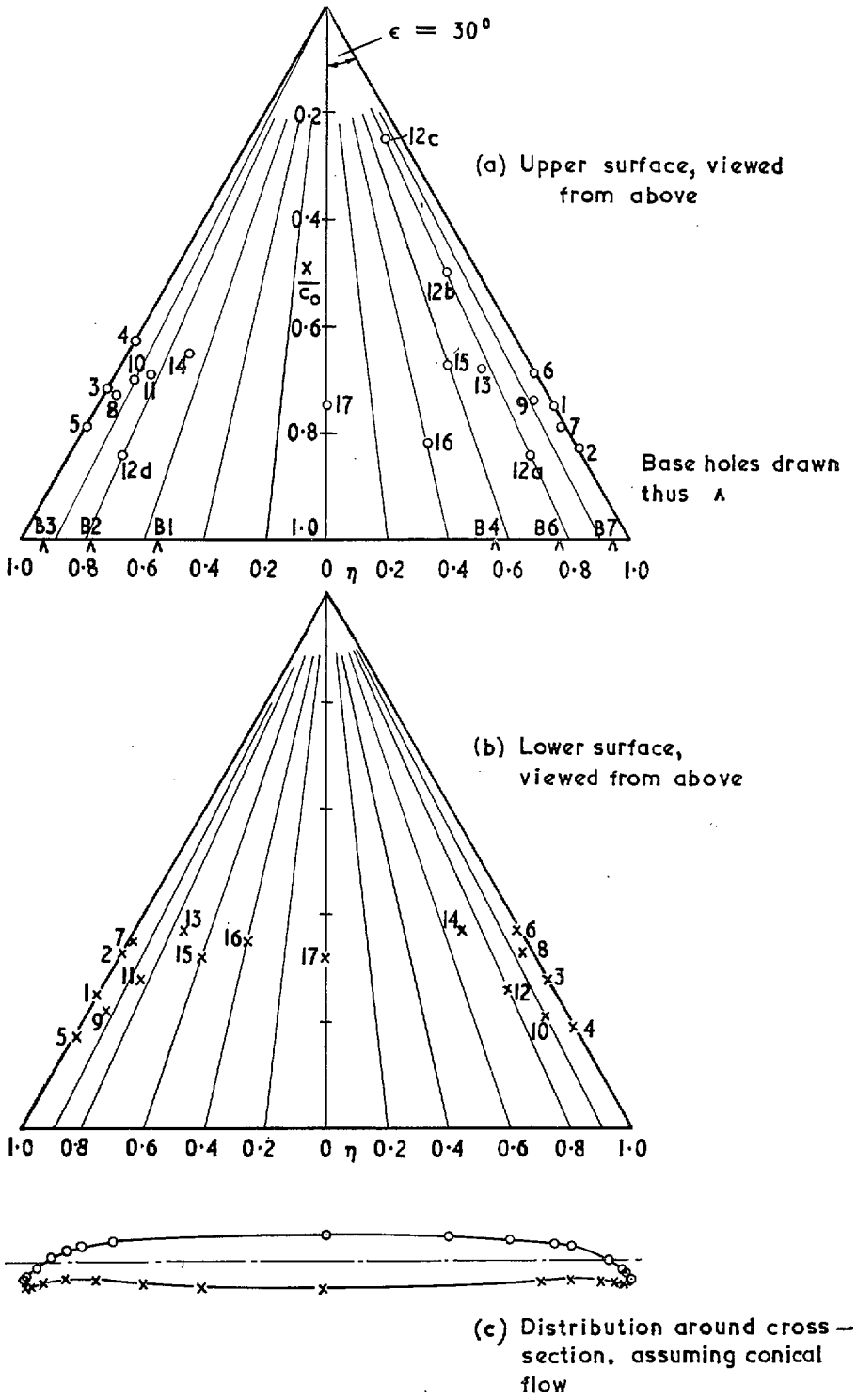

FIG. 3. Distribution of pressure holes on cambered cone.

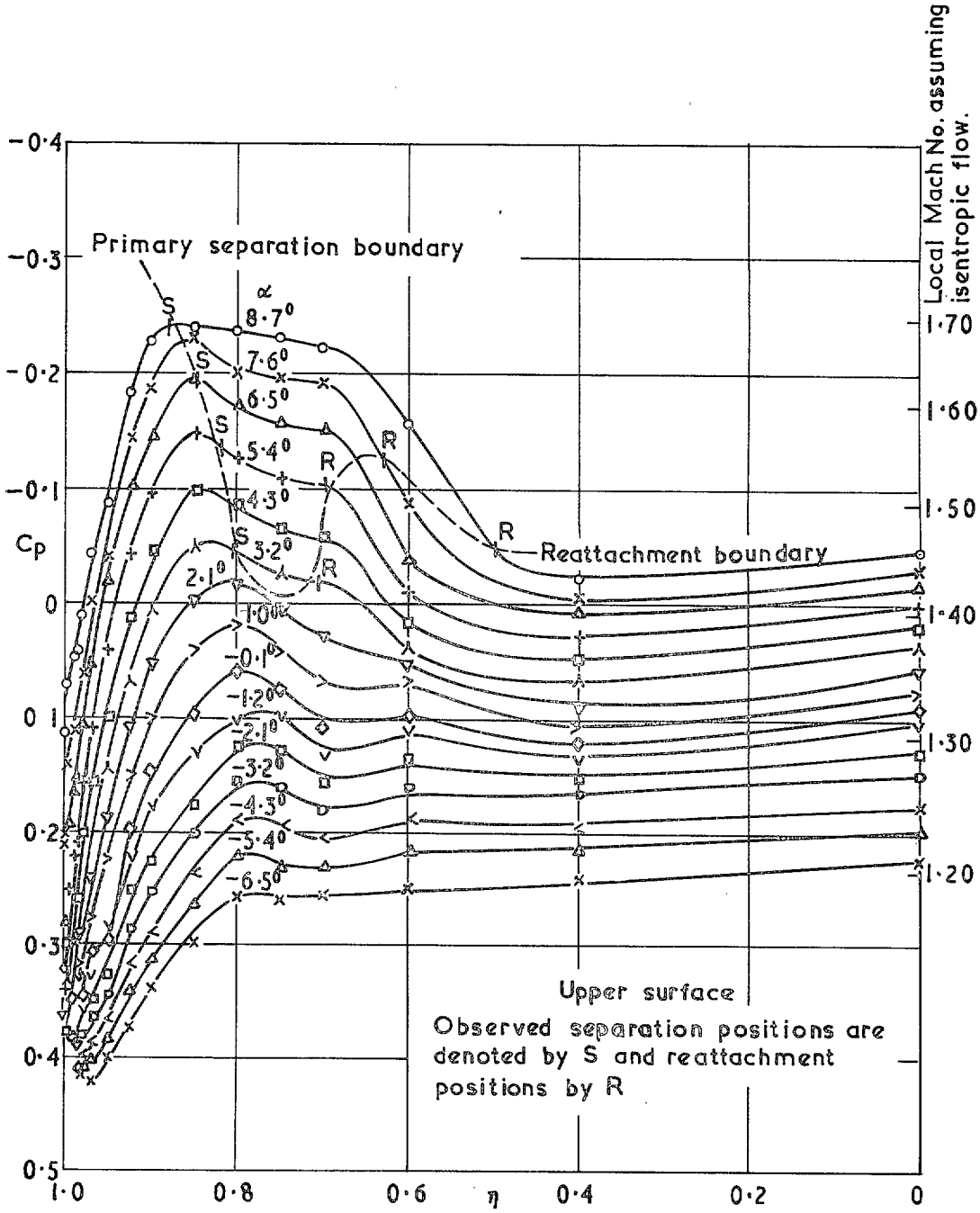

FIG. 4a. Spanwise pressure distribution on upper surface of cambered cone at $M_0 = 1 \cdot 41$ (transition free).

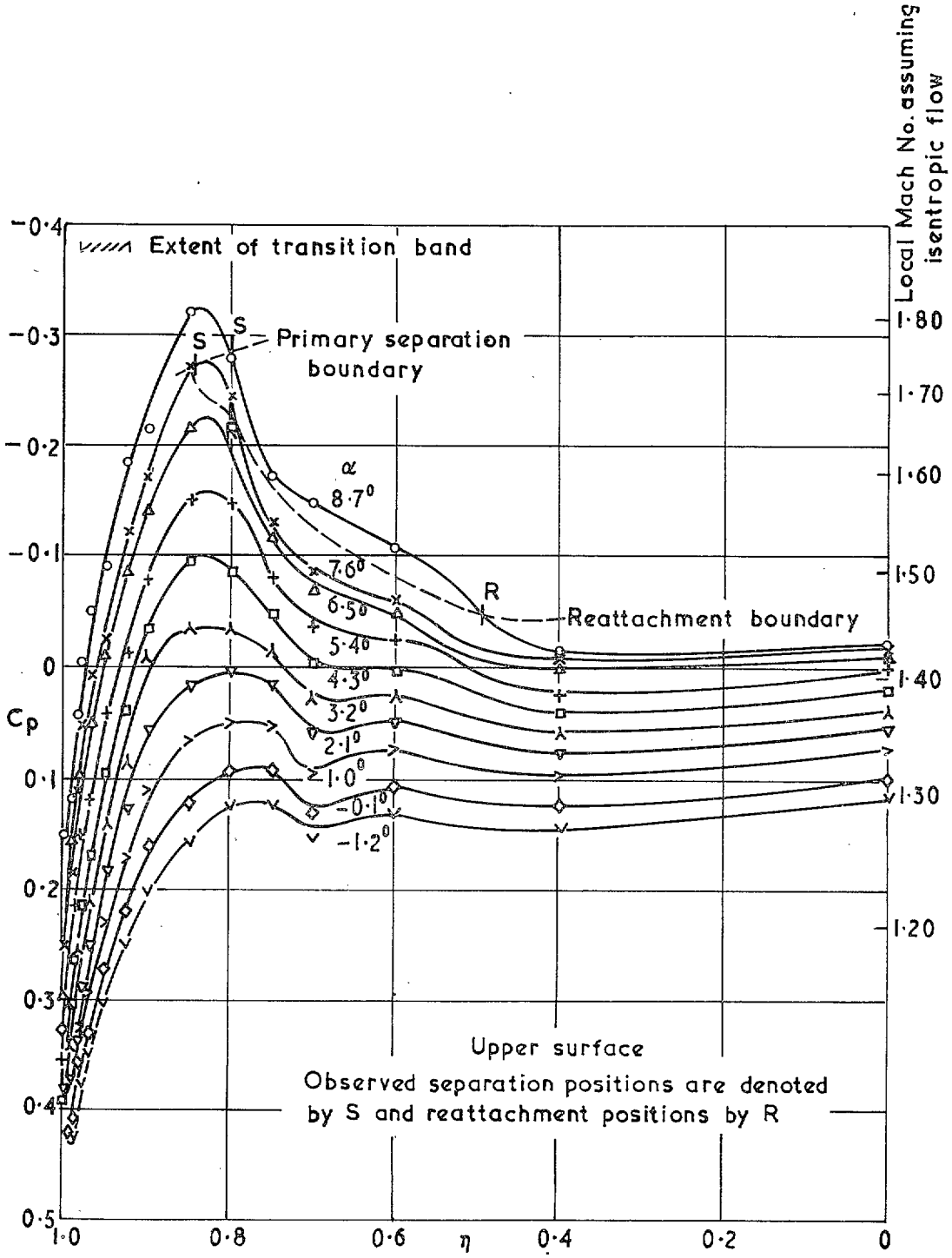

FIG. 4b. Spanwise pressure distribution on upper surface of cambered cone at $M_0 = 1 \cdot 41$ (transition fixed).

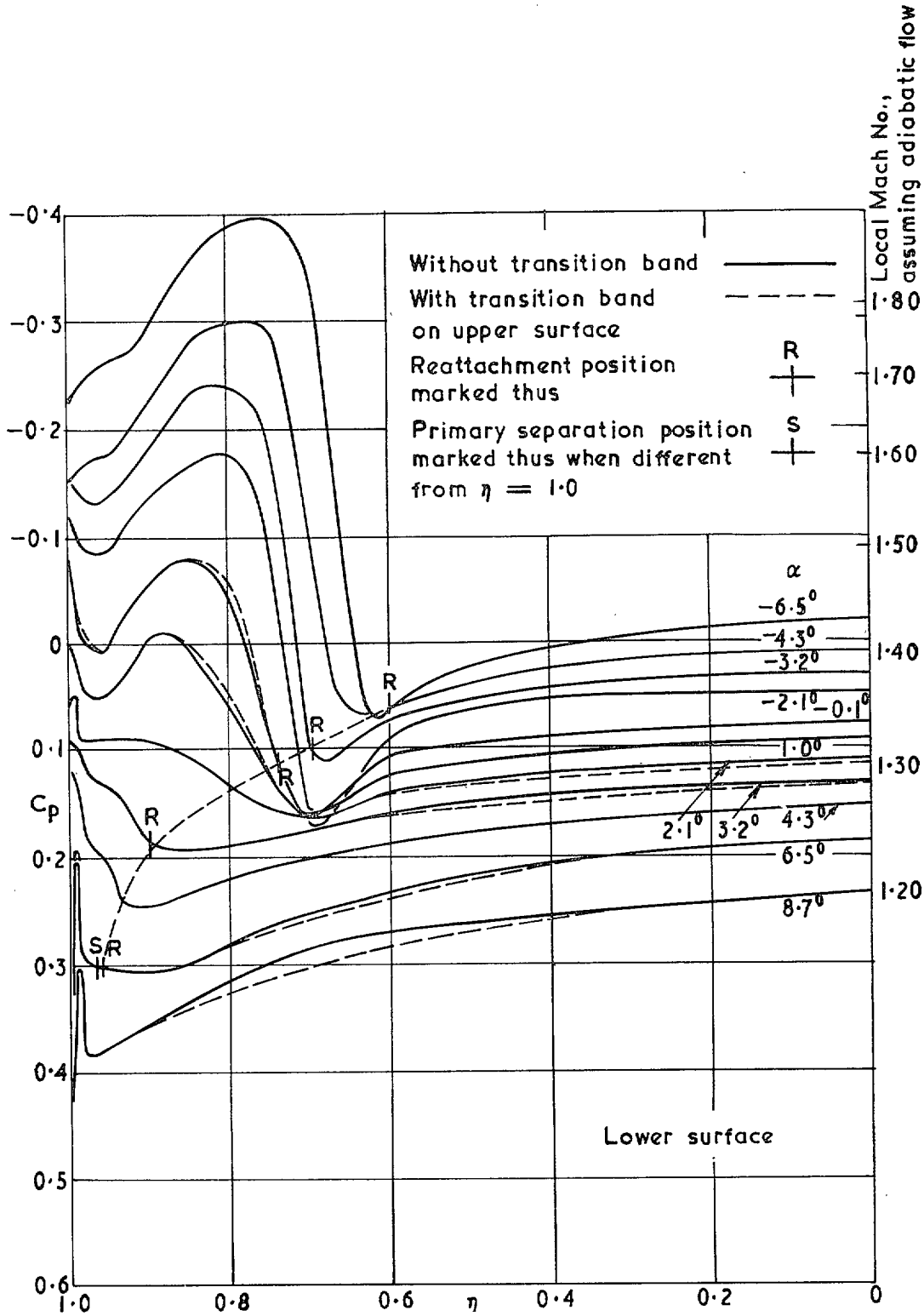

FIG. 4c. Spanwise pressure distributions on lower surface of cambered cone at $M_0 = 1{\cdot}41$.

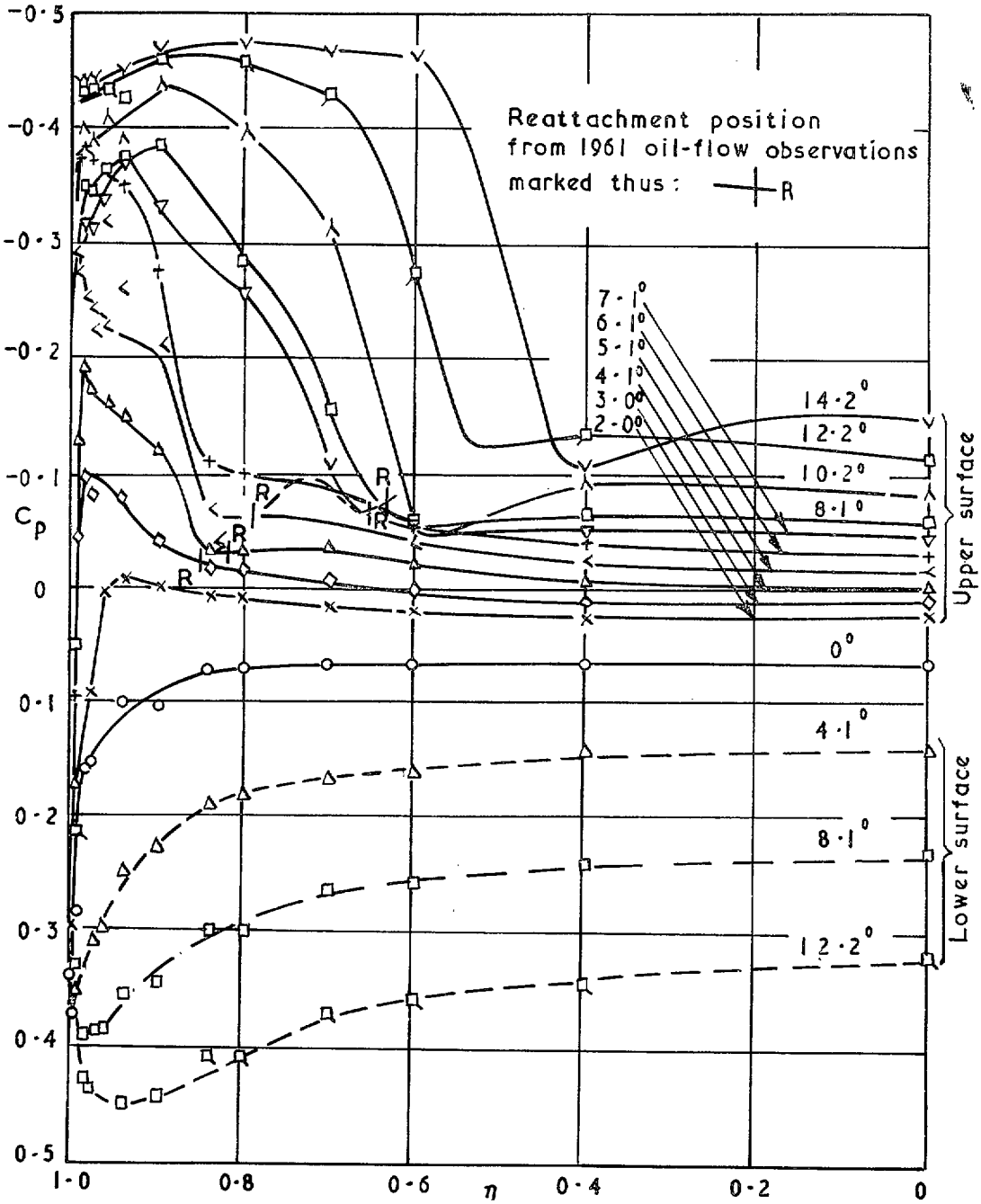

FIG. 5. Pressure distributions on uncambered elliptic cone with no roughness band (1954).

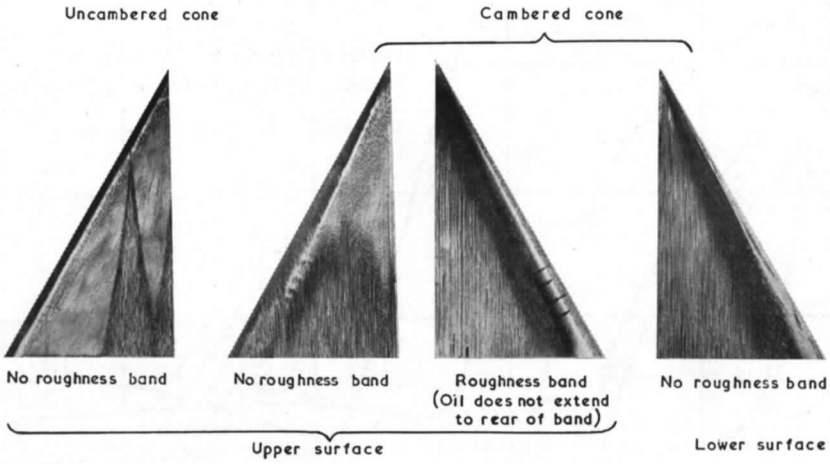

FIG. 6a. Oil patterns at $M_0 = 1 \cdot 41$, $\alpha = 0°$.

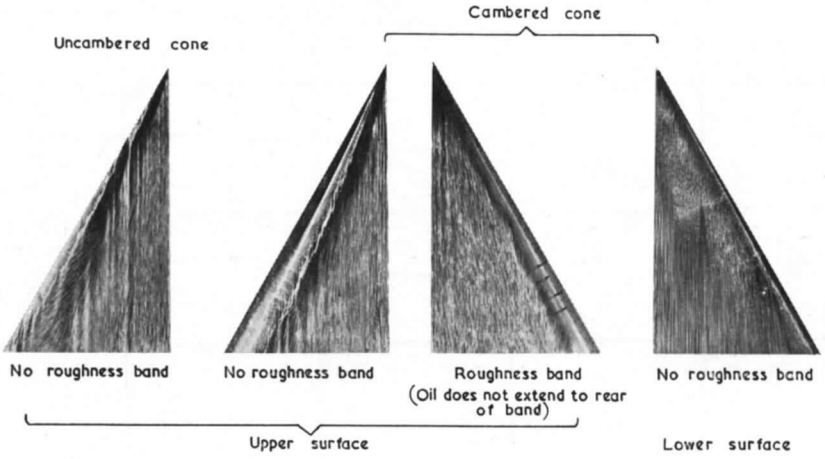

FIG. 6b. Oil patterns at $M_0 = 1 \cdot 41$, $\alpha = 6 \cdot 5°$.

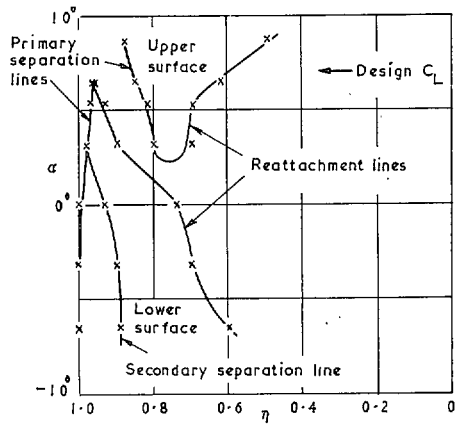

(a) Flow boundaries for cambered cone without roughness band

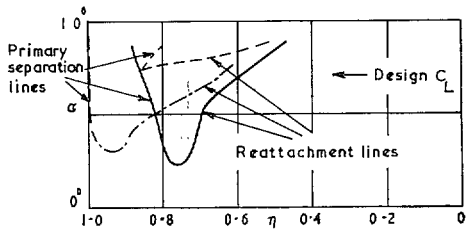

(b) Comparison of upper-surface flow boundaries

Uncambered cone — - —

Cambered cone

No roughness band ———

With roughness band - - - - -

FIGS. 7a and b.

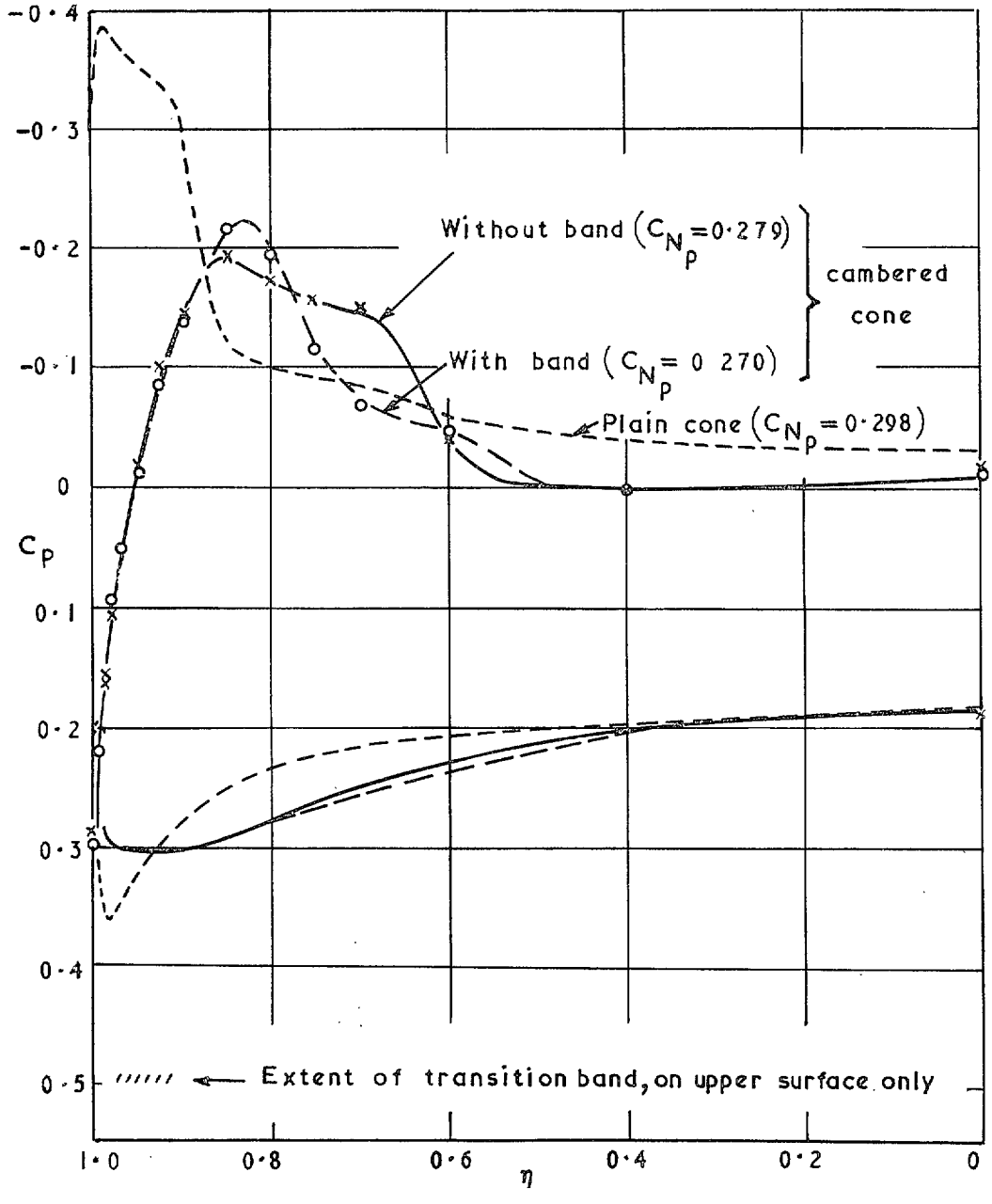

FIG. 8. Comparison of surface pressures near design lift coefficient.

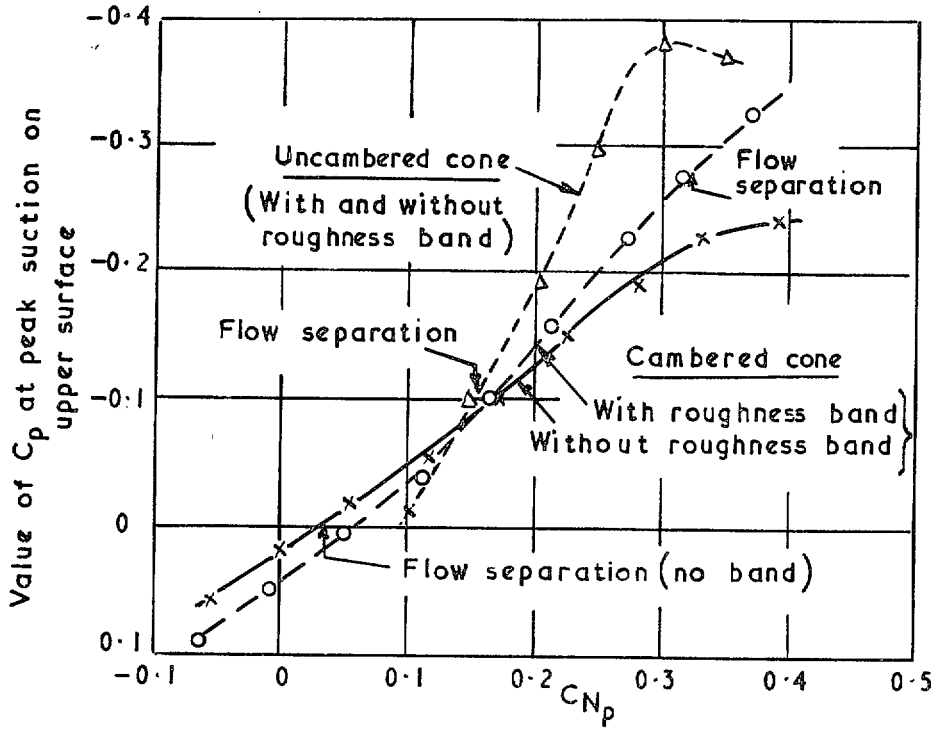

FIG. 9. Variation of minimum value of C_p on upper surface.

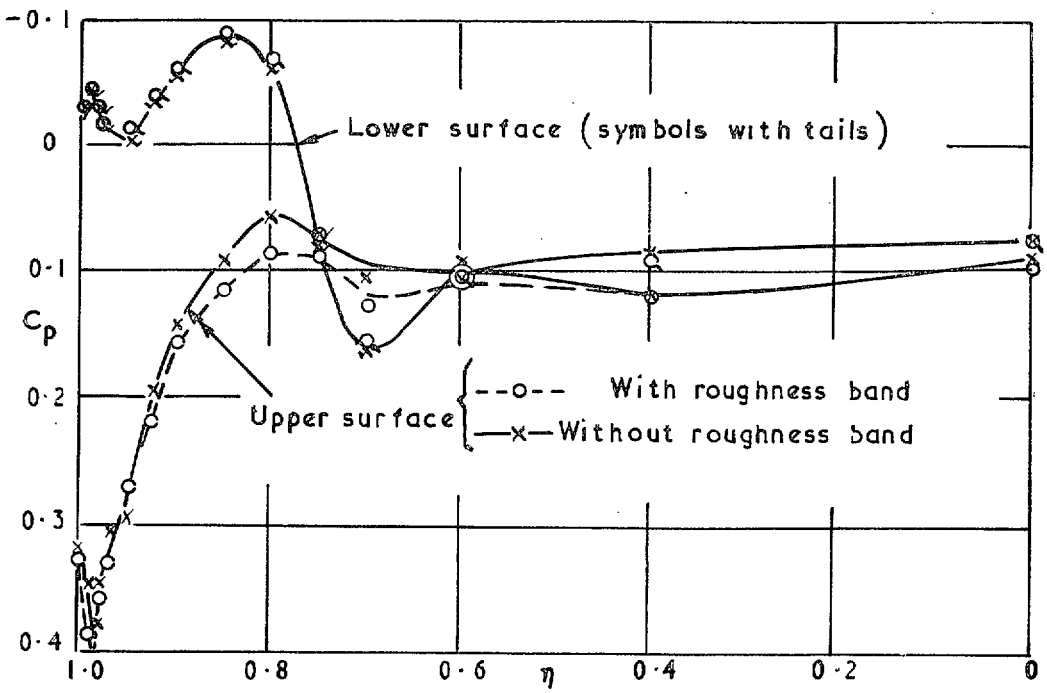

FIG. 10. Comparison of surface pressure distribution on cambered cone with and without roughness band at $\alpha = -0{\cdot}1°$.

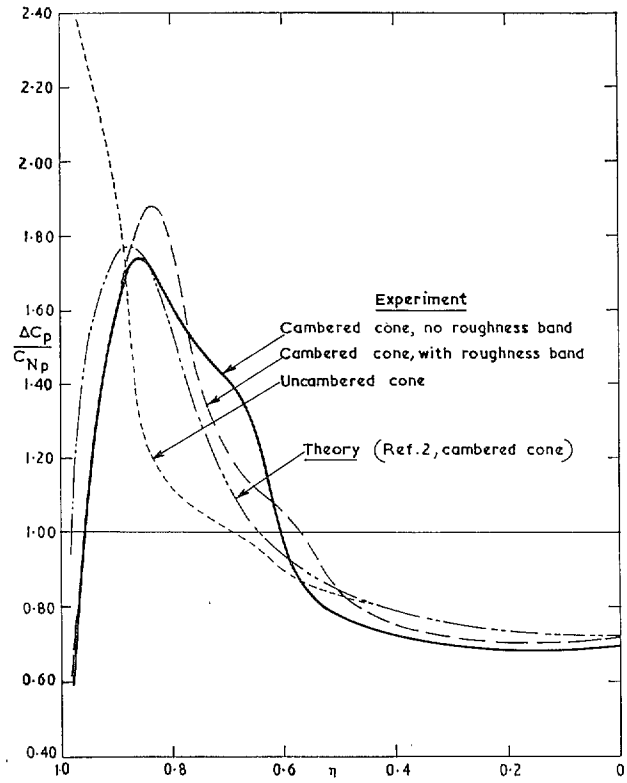

FIG. 11. Comparison of theoretical and experimental loadings near design C_L, based on pressure distributions of Fig. 8.

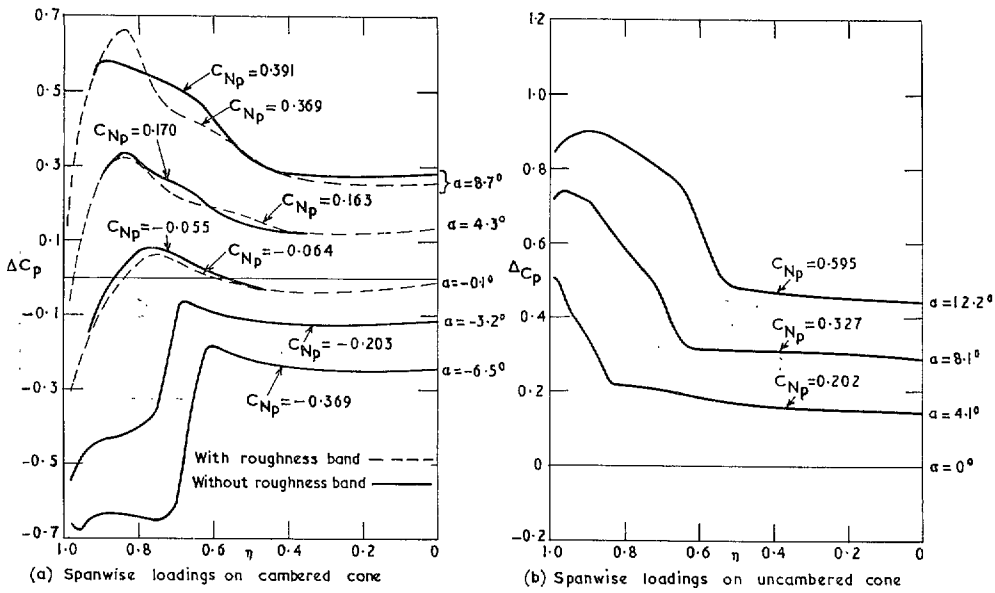

FIGS. 12a and b.

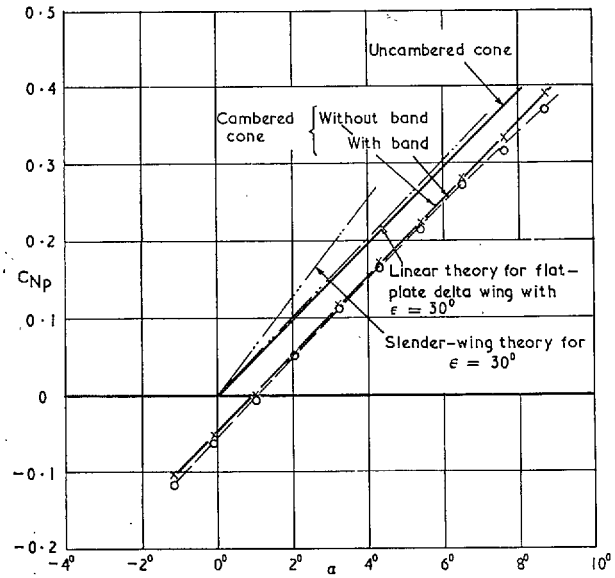

FIG. 13a. Comparison of normal-force coefficients integrated from surface pressures on cambered cone with and without transition band.

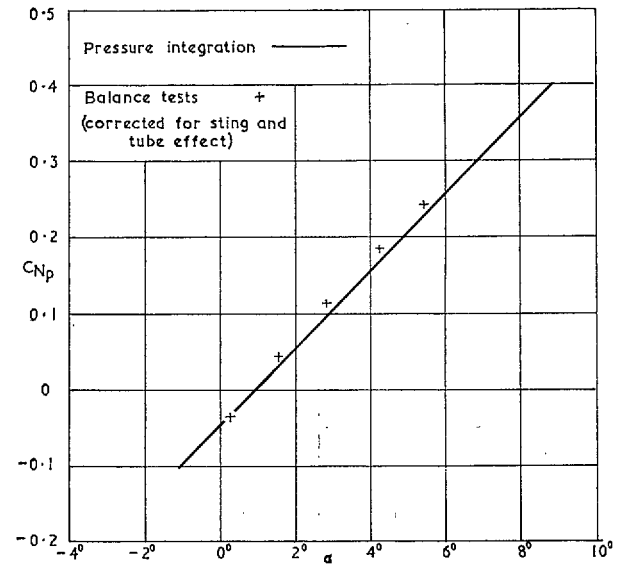

FIG. 13b. Comparison of pressure-integration values of normal force with those measured during balance tests (no roughness band).

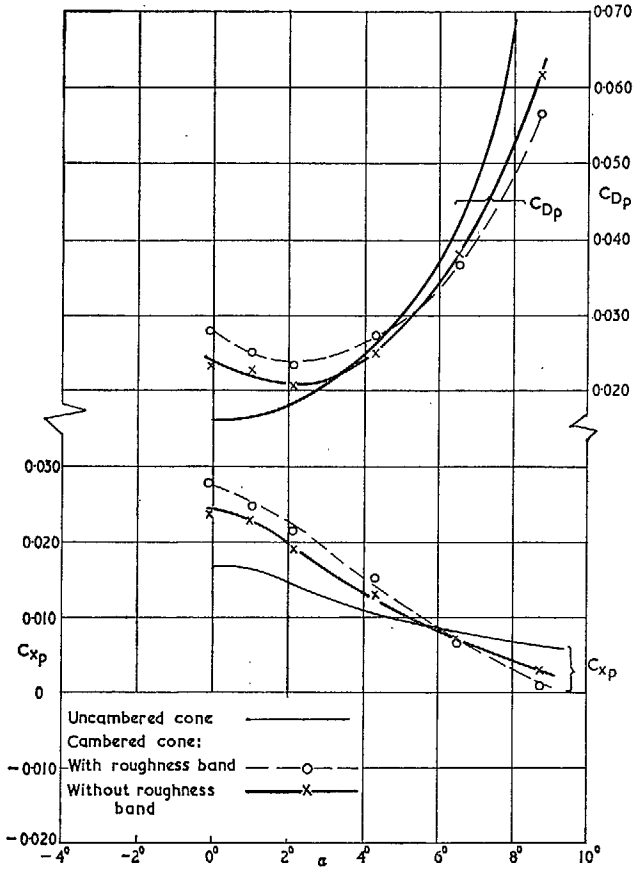

FIG. 14. Comparison of axial and drag pressure-force coefficient.

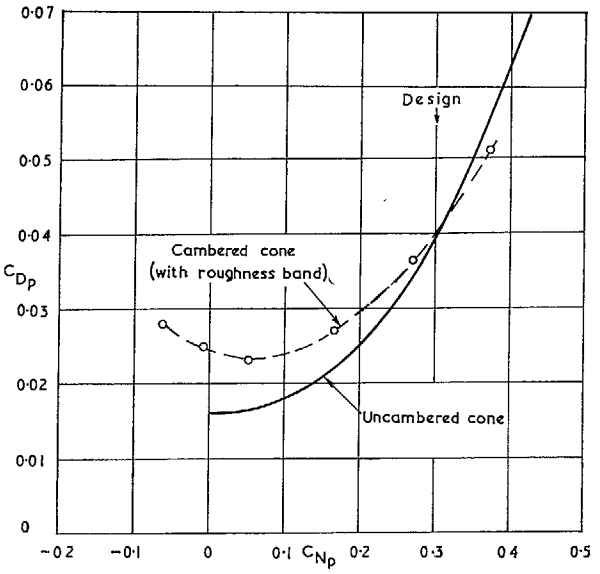

FIG. 15. Pressure-drag curves for cambered and uncambered cones.

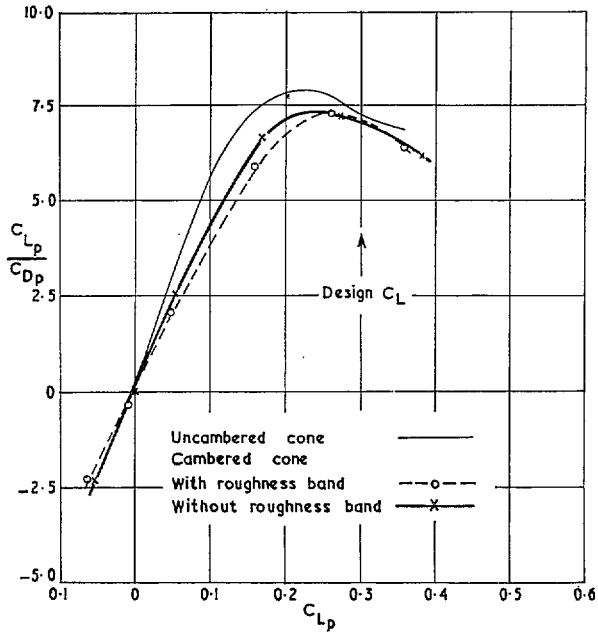

FIG. 16. Comparison of lift/pressure-drag ratio for cambered and uncambered cones.

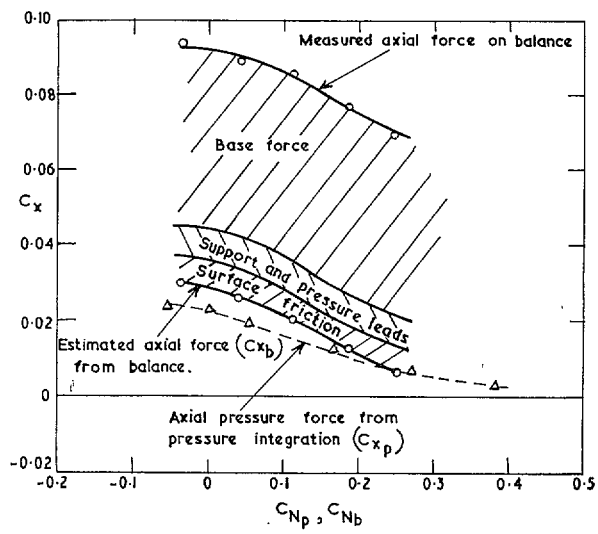

FIG. 17. Comparison of measured and estimated axial pressure force for cambered cone without roughness band.

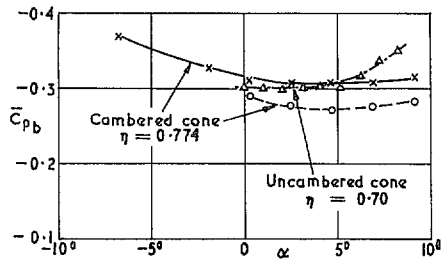

(a) Effect of incidence on base pressure at particular stations

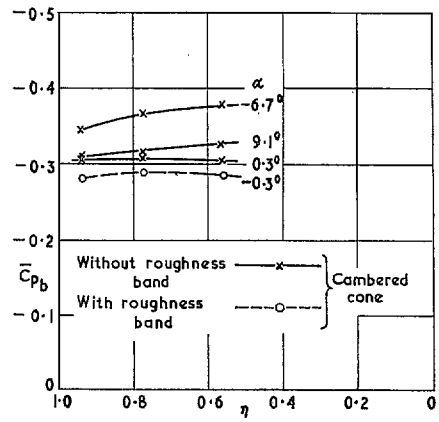

(b) Spanwise variation in base pressure on cambered cone

FIGS. 18a and b.

(86184) Wt. 64/1857 K.5 2/63 Hw.

Publications of the Aeronautical Research Council

ANNUAL TECHNICAL REPORTS OF THE AERONAUTICAL RESEARCH COUNCIL (BOUND VOLUMES)

1942 Vol. I. Aero and Hydrodynamics, Aerofoils, Airscrews, Engines. 75*s.* (post 2*s.* 9*d.*)
Vol. II. Noise, Parachutes, Stability and Control, Structures, Vibration, Wind Tunnels. 47*s.* 6*d.* (post 2*s.* 3*d.*)

1943 Vol. I. Aerodynamics, Aerofoils, Airscrews. 80*s.* (post 2*s.* 6*d.*)
Vol. II. Engines, Flutter, Materials, Parachutes, Performance, Stability and Control, Structures. 90*s.* (post 2*s.* 9*d.*)

1944 Vol. I. Aero and Hydrodynamics, Aerofoils, Aircraft, Airscrews, Controls. 84*s.* (post 3*s.*)
Vol. II. Flutter and Vibration, Materials, Miscellaneous, Navigation, Parachutes, Performance, Plates and Panels, Stability, Structures, Test Equipment, Wind Tunnels. 84*s.* (post 3*s.*)

1945 Vol. I. Aero and Hydrodynamics, Aerofoils. 130*s.* (post 3*s.* 6*d.*)
Vol. II. Aircraft, Airscrews, Controls. 130*s.* (post 3*s.* 6*d.*)
Vol. III. Flutter and Vibration, Instruments, Miscellaneous, Parachutes, Plates and Panels, Propulsion. 130*s.* (post 3*s.* 3*d.*)
Vol. IV. Stability, Structures, Wind Tunnels, Wind Tunnel Technique. 130*s.* (post 3*s.* 3*d.*)

1946 Vol. I. Accidents, Aerodynamics, Aerofoils and Hydrofoils. 168*s.* (post 3*s.* 9*d.*)
Vol. II. Airscrews, Cabin Cooling, Chemical Hazards, Controls, Flames, Flutter, Helicopters, Instruments and Instrumentation, Interference, Jets, Miscellaneous, Parachutes. 168*s.* (post 3*s.* 3*d.*)
Vol. III. Performance, Propulsion, Seaplanes, Stability, Structures, Wind Tunnels. 168*s.* (post 3*s.* 6*d.*)

1947 Vol. I. Aerodynamics, Aerofoils, Aircraft. 168*s.* (post 3*s.* 9*d.*)
Vol. II. Airscrews and Rotors, Controls, Flutter, Materials, Miscellaneous, Parachutes, Propulsion, Seaplanes, Stability, Structures, Take-off and Landing. 168*s.* (post 3*s.* 9*d.*)

1948 Vol. I. Aerodynamics, Aerofoils, Aircraft, Airscrews, Controls, Flutter and Vibration, Helicopters, Instruments, Propulsion, Seaplane, Stability, Structures, Wind Tunnels. 130*s.* (post 3*s.* 3*d.*)
Vol. II. Aerodynamics, Aerofoils, Aircraft, Airscrews, Controls, Flutter and Vibration, Helicopters, Instruments, Propulsion, Seaplane, Stability, Structures, Wind Tunnels. 110*s.* (post 3*s.* 3*d.*)

Special Volumes

Vol. I. Aero and Hydrodynamics, Aerofoils, Controls, Flutter, Kites, Parachutes, Performance, Propulsion, Stability. 126*s.* (post 3*s.*)
Vol. II. Aero and Hydrodynamics, Aerofoils, Airscrews, Controls, Flutter, Materials, Miscellaneous, Parachutes, Propulsion, Stability, Structures. 147*s.* (post 3*s.*)
Vol. III. Aero and Hydrodynamics, Aerofoils, Airscrews, Controls, Flutter, Kites, Miscellaneous, Parachutes, Propulsion, Seaplanes, Stability, Structures, Test Equipment. 189*s.* (post 3*s.* 9*d.*)

Reviews of the Aeronautical Research Council

1939–48 3*s.* (post 6*d.*) 1949–54 5*s.* (post 5*d.*)

Index to all Reports and Memoranda published in the Annual Technical Reports

1909–1947 R. & M. 2600 (out of print)

Indexes to the Reports and Memoranda of the Aeronautical Research Council

Between Nos. 2351–2449	R. & M. No. 2450	2*s.* (post 3*d.*)
Between Nos. 2451–2549	R. & M. No. 2550	2*s.* 6*d.* (post 3*d.*)
Between Nos. 2551–2649	R. & M. No. 2650	2*s.* 6*d.* (post 3*d.*)
Between Nos. 2651–2749	R. & M. No. 2750	2*s.* 6*d.* (post 3*d.*)
Between Nos. 2751–2849	R. & M. No. 2850	2*s.* 6*d.* (post 3*d.*)
Between Nos. 2851–2949	R. & M. No. 2950	3*s.* (post 3*d.*)
Between Nos. 2951–3049	R. & M. No. 3050	3*s.* 6*d.* (post 3*d.*)
Between Nos. 3051–3149	R. & M. No. 3150	3*s.* 6*d.* (post 3*d.*)

HER MAJESTY'S STATIONERY OFFICE

from the addresses overleaf

© *Crown copyright* 1963

Printed and published by
HER MAJESTY'S STATIONERY OFFICE

To be purchased from
York House, Kingsway, London W.C.2
423 Oxford Street, London W.1
13A Castle Street, Edinburgh 2
109 St. Mary Street, Cardiff
39 King Street, Manchester 2
50 Fairfax Street, Bristol 1
35 Smallbrook, Ringway, Birmingham 5
80 Chichester Street, Belfast 1
or through any bookseller

Printed in England

S.O. Code No. 23-3306